

¹Key Laboratory of Automobile Materials of MOE and School of Materials Science and Engineering, Jilin University, Changchun 130012, China; ²Department of Chemical and Biomolecular Engineering, Yonsei University, Seoul 03722, Republic of Korea; ³Department of Materials Science and Engineering, Korea Advanced Institute of Science and Technology (KAIST), Daejeon 34141, Republic of Korea; ⁴College of Chemistry, Jilin University, Changchun 130012, China; ⁵School of Energy and Chemical Engineering, Ulsan National Institute of Science and Technology (UNIST), Ulsan 44919, Republic of Korea; ⁶Pritzker School of Molecular Engineering, The University of Chicago, Chicago, IL 60637, USA and ⁷Department of Battery Engineering, Yonsei University, Seoul 03722, Republic of Korea

*Corresponding authors. E-mails: souldotcom@unist.ac.kr; dseo@kaist.ac.kr; syleek@yonsei.ac.kr

†Equally contributed to this work.

Received 7 January 2025; Revised 5 May 2025; Accepted 14 May 2025

MATERIALS SCIENCE

Ion channel-gated covalent organic framework membrane for sustainable lithium–sulfur batteries

Zhongping Li^{1,2,†}, Jae-Seung Kim^{3,†}, Hyunseok Moon^{2,†}, Kyeong-Seok Oh², Yuxin Hou⁴, Sodam Park^{5,*}, Kun Ryu⁶, Changqing Li⁵, Jeong-Min Seo⁴, Xiaoming Liu⁴, Jong-Beom Baek⁵, Dong-Hwa Seo^{3,*} and Sang-Young Lee^{2,7,*}

ABSTRACT

Lithium–sulfur (Li–S) batteries hold promise as a compelling alternative to current state-of-the-art Li-ion batteries due to their high theoretical capacity, low cost and the natural abundance of sulfur. However, the practical realization of Li–S batteries has been plagued by the longstanding trade-off issue between polysulfide shuttle suppression and Li⁺ transport. Here, we report an ion channel-gated covalent organic framework (COF) as an ionic diode membrane strategy to address this conflicting requirement. By tuning the chemical structure of tethered anions, the resulting COF features 1D anionic channels with optimized charge delocalization and pore size. The bulky anions enhance Li⁺ dissociation and conduction while effectively repelling polysulfides dissolved from S cathodes. Additionally, the COF ionic diode mitigates self-discharge and inhibits parasitic reactions. Consequently, Li–S cells assembled with the COF ionic diode improve charge/discharge capacities and cycle life under constrained operating conditions.

Keywords: anionic covalent organic frameworks, ion channel, ionic sieve membrane, charge delocalization, dissociation of Li⁺, Li–S batteries

INTRODUCTION

The ever-increasing demand for advanced batteries with high energy density and a long cycle life has inspired the relentless pursuit of new electrochemical systems and electrode materials. However, there are challenges associated with augmenting the charge storage capability of intercalation-based transition metal oxide cathodes, which are prevalently used in current state-of-the-art Li-ion batteries, as well as enhancing their performance to meet the evolving requirements of the competitive markets [1–3]. Consequently, this has prompted extensive research into alternative cathode materials. Owing to its high theoretical capacity (1672 mAh g^{−1}), low cost, environmental friendliness and natural abundance, sulfur has been proposed as a promising cathode material [4,5].

Despite the notable benefits of Li–S batteries [6,7], several challenges, particularly the ‘shuttle effect’ of Li polysulfides (PSs), have hindered their practical application. Accordingly, numerous research efforts have been devoted to resolving the

problem of the PSs shuttle effect [8–11], including the modifications of sulfur cathodes [12–17], electrolyte engineering [18,19] and the protection of Li-metal anodes [20,21]. However, these methods often fail to effectively suppress diffusion of PSs, resulting in poor capacity retention. Moreover, the increased proportion of inactive cell components and the complex processability hinder their practical viability. In contrast to the aforementioned approaches, membranes incorporating functional layers, such as carbon [22–24], inorganic [25–27] and hybrids [28,29], have attracted considerable attention due to their high selectivity for PSs, resulting in improved cyclability. However, these approaches often lead to a compromise between inhibiting the PSs shuttle effect and facilitating Li⁺ conduction. This trade-off becomes particularly pronounced under constrained electrolyte conditions (e.g. low electrolyte-to-sulfur (E/S) ratios of <5 μL mg_{sulfur}^{−1}) and in high-capacity cells (>5 mAh cm^{−2}). Therefore, there is an urgent need to develop a new membrane concept that can effectively suppress the PSs shuttle

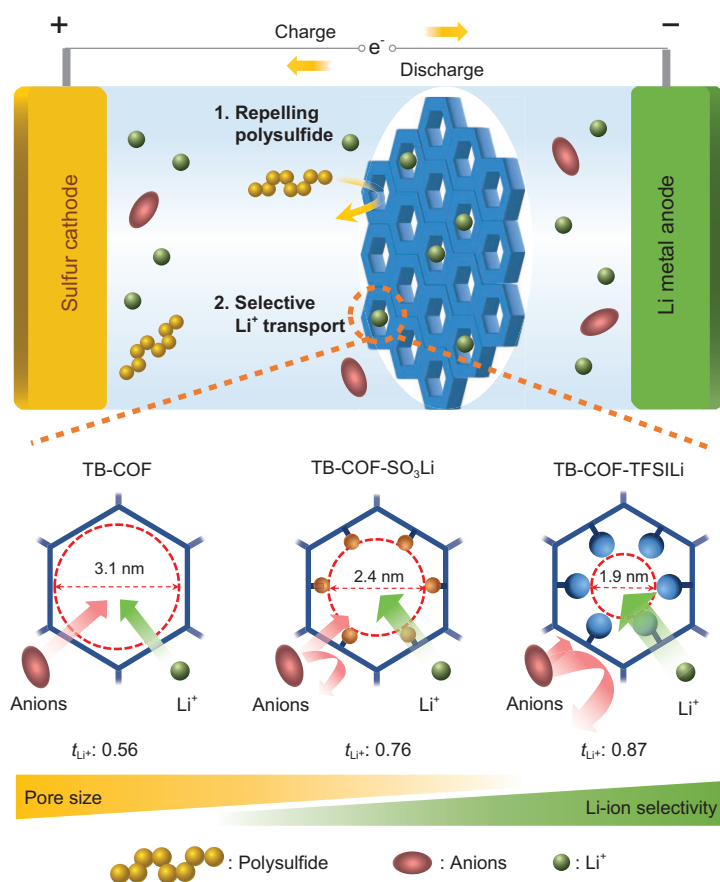


Figure 1. Schematic illustration of the fabrication of anionic COFs as an ionic sieve membrane for Li-S batteries.

effect without impairing the Li^+ transport phenomena. Among the many membrane materials reported to date, covalent organic frameworks (COFs) [30–36] have recently emerged as a promising membrane material owing to their directional porous structure, structural stability and chemical tunability [37–50,51]. Additionally, from a battery perspective, the functional and aligned 1D pore channels of COFs are expected to enable chemical selectivity and facilitate charge transport [52–55].

In this study, an ion channel-gated COF with charge-delocalized, narrowed pores is introduced as a class of ionic diode membranes to address the persistent trade-off challenge between the PSs shuttle prevention (selectivity) and Li^+ conduction (permeability) (Fig. 1). The charge delocalization and pore size of the anionic channels were regulated by varying the chemical structure of tethered anions. Particularly, imine-containing COFs were synthesized with different anions (sulfonate (SO_3^-) and bis(trifluoromethane)sulfonimide (TFSI $^-$)). Whereas previous studies have primarily focused on attaching functional groups to the COF skeletons [50,56–59], we aimed to regulate the pore size and

charge density distribution of anionic COF channels by incorporating ionic groups inside the COFs. The incorporation of a bulky anion (TFSI $^-$) into the COF channels facilitated charge delocalization and pore-size reduction, thereby effectively repelling polysulfides through a synergistic combination of electrostatic interactions and steric hindrance. Furthermore, the delocalized negative charge distribution suppressed anion transport while promoting Li^+ dissociation, enabling highly selective (transference number of Li^+ $t_{\text{Li}^+} = 0.87$) and efficient Li^+ conduction through the COF channels.

RESULTS AND DISCUSSION

Structure and characterization of ion channel-gated COFs

In this study, an imine-based TB-COF was first synthesized by mixing 2,5-bis(prop-2-yn-1-yloxy) terephthalaldehyde (BPTA) and 2,4,6-tris(4-aminophenyl)-1,3,5-triazine (TAPT) in a solution of dioxane and mesitylene with 6 M acetic acid used as a catalyst for 3 days at 120°C. Thereafter, the highly charged TB-COF- SO_3Li and TB-COF-TFSILi were synthesized by post-functionalization of the channel walls of the pre-synthesized TB-COF (for details, see Fig. 2a and experimental section, Notes S1–S3). The morphologies of the obtained TB-COF, TB-COF- SO_3Li and TB-COF-TFSILi were characterized (Figs S1 and S2). Overall, no significant difference in the morphologies of these COFs was observed, indicating that the post-functionalization of the TB-COF did not affect the morphologies of the resulting modified COFs. Signals corresponding to the imine bond and tri-bond were observed in the Fourier transform infrared (FT-IR) spectra of TB-COF at 1576 and 2129 cm^{-1} , respectively (Fig. S3, green). Additionally, a strong peak was observed in the ^{13}C magic angle spin solid-state nuclear magnetic resonance (NMR) of TB-COF at 160.4 ppm, corresponding to the carbon atoms within the imine linkage (Fig. S4a). Furthermore, notable carbon peaks of the tri-bond were observed at 72.4 and 78.3 ppm. After the post-synthesis, the tri-bond signals within the FT-IR spectra of TB-COF- SO_3Li (Fig. S3, orange) and TB-COF-TFSILi (Fig. S3, blue) were dispersed. In addition, the carbon signal of the tri-bond disappeared and new peaks from triazine units emerged at 143.1 ppm (Fig. S4b). Further, a strong peak was observed at –71.5 ppm, which corresponded to the fluorine atoms of TB-COF-TFSILi (Fig. S4c). The surface chemistry of TB-COFs was analysed by using X-ray photoelectron spectroscopy (XPS), which revealed different element

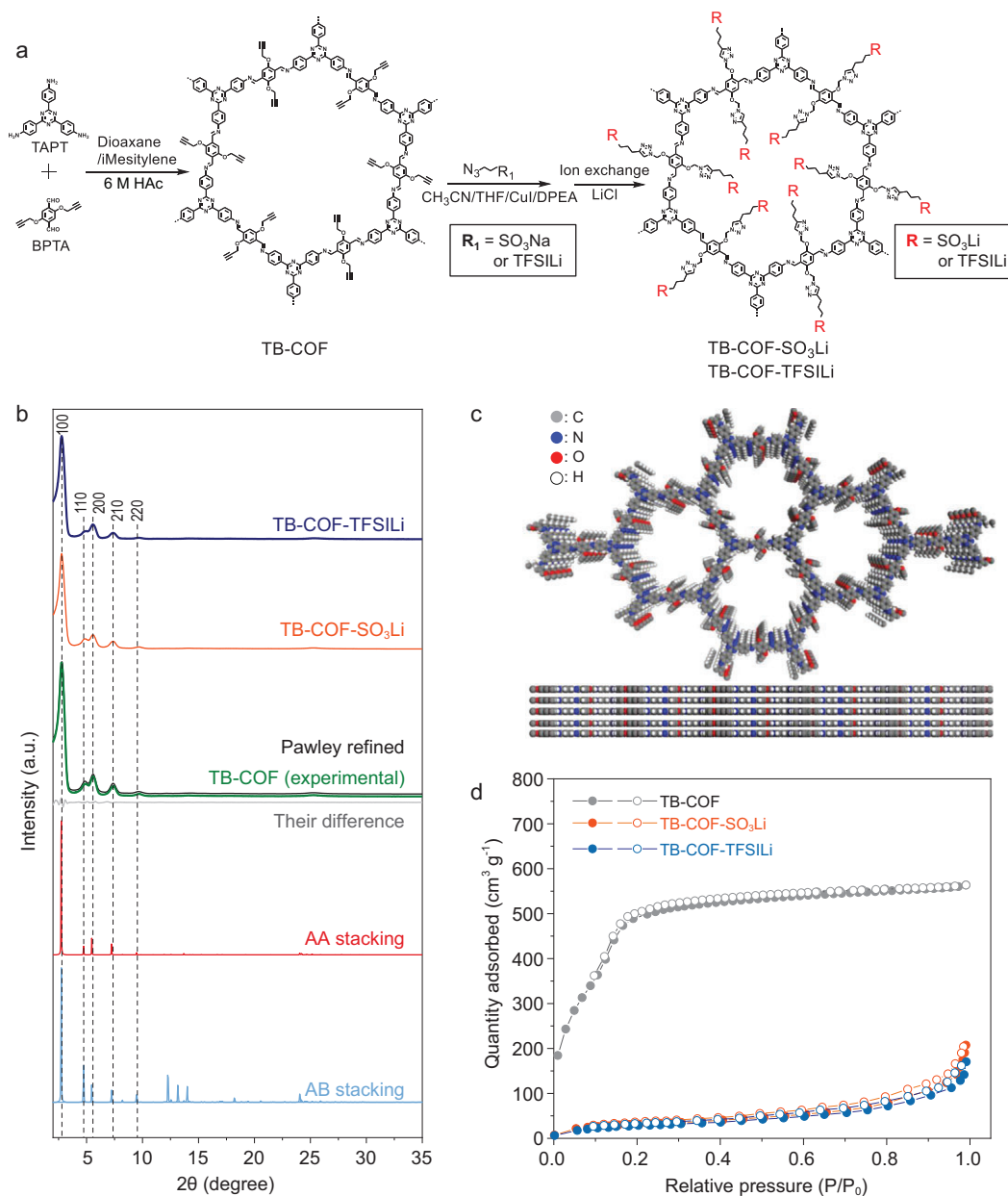


Figure 2. Structure and characterization of the TB-COF, TB-COF-SO₃Li and TB-COF-TFSiLi. (a) Synthetic scheme of COFs. (b) Experimental and theoretical PXRD patterns. (c) Theoretical unit cells of the TB-COF. (d) Nitrogen sorption isotherms measured at 77 K (solid: adsorption; hollow: desorption).

distributions. The peaks of carbon (C 1s), nitrogen (N 1s), oxygen (O 1s), sulfur (S 2p), and lithium (Li 1s) were observed in the XPS profiles of TB-COF, TB-COF-SO₃Li and TB-COF-TFSiLi (Fig. S5a–c). Particularly, the TB-COF-TFSiLi showed a strong peak of F 1s at 668.0 eV, indicating the presence of TFSi[−] as a tethered anion (Fig. S5c). Meanwhile, a characteristic peak of Cl 1s at 199 eV was not detected at both the TB-COF-SO₃Li and TB-COF-TFSiLi, exhibiting the successful removal of LiCl during the ion-exchange step.

The crystalline properties of COFs were investigated by using powder X-ray diffraction (PXRD)

measurements. The PXRD pattern of TB-COF exhibited distinct diffraction peaks at 2.78° (100), 4.90° (110), 5.58° (200), 7.38° (210), 9.72° (220) and 25.24° (001), confirming its high crystallinity (Fig. 2b, green). After Pawley refinement, the observed PXRD pattern matched well with the simulated patterns from the AA-staggered stacking model (Fig. 2b, red). The optimized cell parameters of TB-COF showed good agreement factors ($R_p = 2.77\%$, $R_{wp} = 3.78\%$, $a = b = 37.3302 \text{ \AA}$, $c = 3.6985 \text{ \AA}$, $\alpha = \beta = 90^\circ$ and $\gamma = 120^\circ$, Fig. 2c). The TB-COF-SO₃Li (Fig. 2b, orange) and TB-COF-TFSiLi (Fig. 2b, blue) also maintained

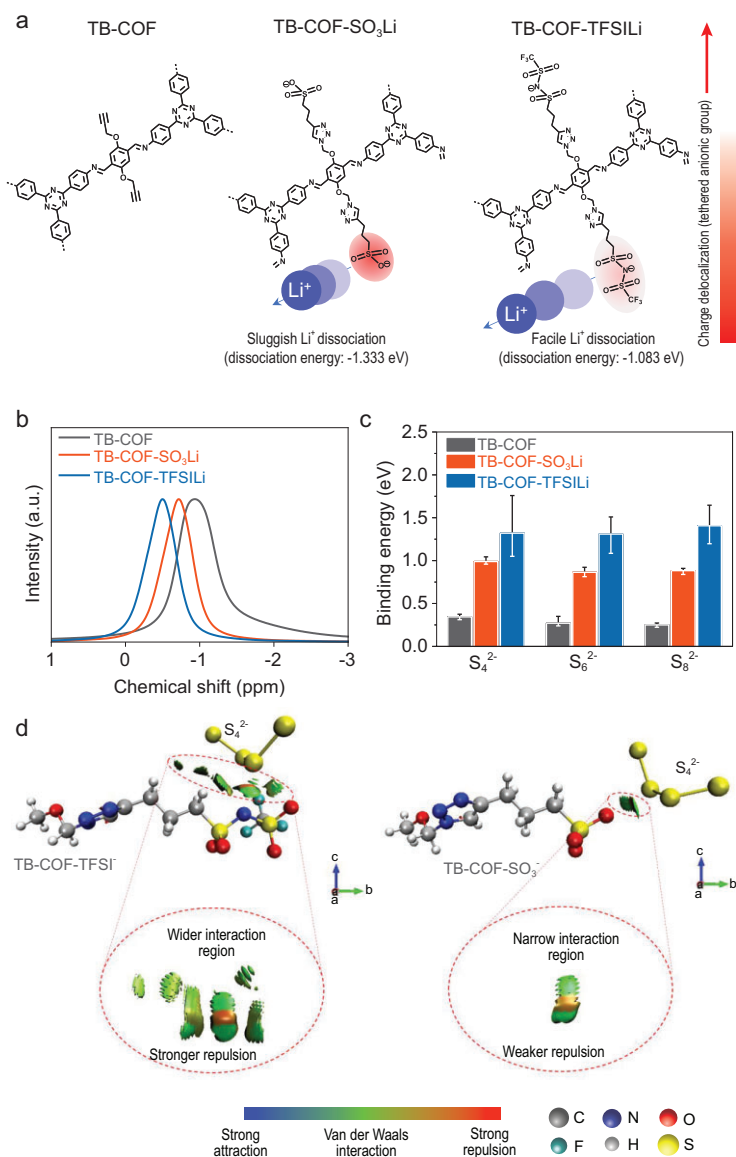


Figure 3. Effect of tethered anions in the COFs on Li^+ dissociation and interaction with PSs. (a) Chemical structures of the weaker ion correlations expected in systems employing larger ions with greater charge delocalization. The degree of correlation is shown by the scale bar on the right. (b) Solid-state ^7Li NMR spectra of COFs. (c) Gibbs free energy of binding between COFs and S_n^{2-} . The main color bar represents the median binding energy value, calculated from 20 structures of each functional motif in COFs and each PSs composition. Additionally, the gray error bars indicate the range of binding energy values. (d) Non-covalent interactions within 3D molecular structures of the functional group in the TB-COF and PSs. TB-COF-TFSiLi- S_4^{2-} (left) and TB-COF- SO_3Li - S_4^{2-} (right).

a high crystallinity. The specific surface area was determined by using the Brunauer–Emmett–Teller method (Fig. 2d). TB-COF exhibited a high surface area of $1728 \text{ m}^2 \text{ g}^{-1}$ [1]. In comparison, TB-COF- SO_3Li and TB-COF-TFSiLi revealed lower surface areas of 81 and $72 \text{ m}^2 \text{ g}^{-1}$ [1], respectively. In addition, the pore-size distribution of the COFs was analysed by using N_2 adsorption–desorption

isotherms (Fig. S6). The average pore-size values of the TB-COF, TB-COF- SO_3Li and TB-COF-TFSiLi were estimated to be 3.1, 2.4 and 1.9 nm, respectively. We confirmed that the average pore sizes of these COFs are consistent with the theoretical density functional theory (DFT) values obtained from the calculation of six-layer stacked COFs. It was observed that the cross-sectional area of TB-COF-TFSiLi (240.0 \AA^2) was lower than those of TB-COF- SO_3Li (433.0 \AA^2) and TB-COF (744.0 \AA^2) (Table S1). As the volumetric flow rate of molecules is directly proportional to the cross-sectional area according to Darcy's law [60], the reduced channel dimensions in TB-COF-TFSiLi effectively suppress the transport of bulky PSs and TFSi $^-$ anions, thereby enhancing the ion-sieving effect. These results confirm that TB-COF-TFSiLi was successfully synthesized via wall-channel functionalization, demonstrating its ability to selectively regulate ion transport while mitigating polysulfide crossover.

Effect of tethered anions in COFs on Li^+ dissociation and interaction with PSs

DFT calculations were performed to evaluate the dissociation energy between Li^+ and the $-\text{SO}_3^-$ and $-\text{TFSi}-\text{COF}$ motifs. The dissociation energy of SO_3Li (-1.333 eV) was higher than that of TFSiLi (-1.083 eV) (Fig. 3a and Fig. S7), indicating that Li^+ dissociates more readily from TFSi $^-$ than from SO_3^- . To further investigate the charge distribution, molecular electrostatic potential (MESP) plots of the functional groups were analysed (Fig. S8). Delocalized negative charge sites were observed in the patterns of TFSi $^-$, whereas the patterns of $-\text{SO}_3^-$ presented a high charge density and negative potential. Consequently, the dissociation of Li^+ from SO_3^- is expected to be more challenging. Next, the local chemical environment of Li^+ in the COFs was investigated by using ^7Li NMR spectroscopy (Fig. 3b). The ^7Li NMR spectra revealed that TB-COF-TFSiLi demonstrated a narrower peak width compared with TB-COF and TB-COF- SO_3Li , indicating the enhanced mobility of free Li^+ . Additionally, there was a downshift in the ^7Li NMR peak, suggesting the effective dissociation of Li salts [53,54].

Subsequently, the interactions between the functional groups of COFs and PS anions (S_n^{2-}) were investigated by using DFT calculations (Fig. 3c and Fig. S9). The results revealed that TB-COF-TFSiLi exhibited a pronounced tendency for repulsive interactions with PS compared with TB-COF- SO_3^- . We further employed non-covalent interaction

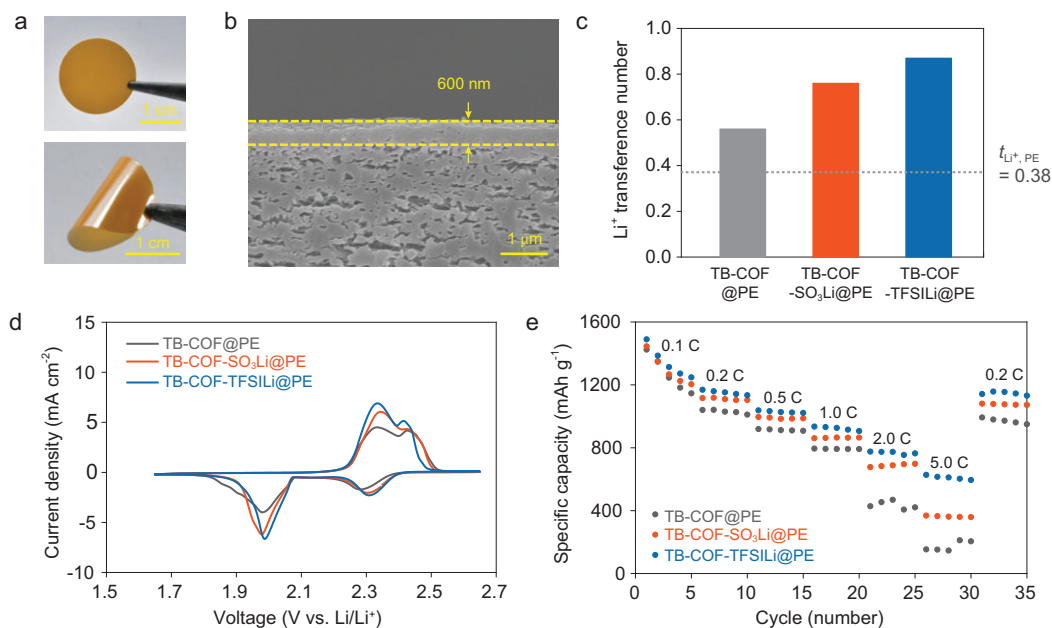


Figure 4. Ion-transport phenomena of the COF membranes. (a) Optical images of the TB-COF-TFSiLi@PE. (b) Cross-sectional SEM image of the TB-COF-TFSiLi@PE. (c) Li⁺ transference number of the pristine PE and various COF@PEs. (d) Comparison of the CV curves of Li-S cells with the COF@PEs. (e) Rate performance of the COF@PEs (sulfur loading = 1.0 mg cm⁻²; E/S ratio = 10 μ L mg⁻¹ sulfur).

(NCI) calculations to obtain the 3D mapping of these interactions (Fig. 3d). The NCI calculations intuitively revealed the attractive and repulsive forces between molecules. Remarkably, TB-COF-TFSi⁻ displayed wider interaction regions and stronger repulsive interactions with PS, suggesting that the presence of a larger, bulky anionic functional group facilitated enhanced repulsion against PS. In particular, the delocalized charge density distribution and the steric hindrance of the bulky TFSi⁻ anion effectively repelled the PS anions.

Transport phenomena of ion-channel-gated COF

The as-synthesized COF was coated on a polyethylene (PE) separator to obtain COF@PE, which was characterized by a yellow color on the COF-coated side (Fig. 4a, top). The COF@PE demonstrated superior flexibility, with no noticeable delamination, even after bending (Fig. 4a, bottom). Scanning electron microscopy (SEM) images of the COF@PE revealed that the PE separator was uniformly covered by the compactly packed COF layer (Fig. S10). The thickness of the COF layer was ~600 nm (Fig. 4b). To verify the electrolyte wettability of the TB-COF-TFSiLi@PE, contact-angle measurement was conducted by dropping a liquid electrolyte (1 M LiTFSi in 1,3-dioxolane (DOL) / 1,2-dimethoxyethane (DME) + 2 wt% LiNO₃) on the pristine PE and

TB-COF-TFSiLi@PE (Fig. S11). The TB-COF-TFSiLi@PE showed a smaller contact angle (19.0°) compared with the pristine PE (25.8°), indicating its improved electrolyte wettability. This improvement can be attributed to the affinity of the negatively charged framework of TB-COF-TFSiLi towards the polar electrolyte.

To demonstrate the effect of anionic charge delocalization, the ionic conductivities of the COF pellets as well as those of the COF@PE were analysed after impregnation with a liquid electrolyte (1 M LiTFSi in DOL/DME = 1/1 (v/v)). The ionic conductivities of the COF pellets at room temperature tended to increase in the following order: TB-COF (1.56×10^{-4} S cm⁻¹), TB-COF-SO₃Li (3.68×10^{-4} S cm⁻¹) and TB-COF-TFSiLi (6.16×10^{-4} S cm⁻¹) (Fig. S12). This result indicates that the delocalized negative charge of the TB-COF-TFSiLi can contribute to the enhancement of ion conduction, which is consistent with the MESP plots obtained from the DFT calculation (Fig. S8) and ⁷Li NMR spectra (Fig. 3b). A similar trend was observed in the ionic conductivity of the COF@PE. The TB-COF-TFSiLi@PE showed higher ionic conductivity (3.77×10^{-4} S cm⁻¹) than the TB-COF-SO₃Li@PE (3.61×10^{-4} S cm⁻¹) and the TB-COF@PE (3.54×10^{-4} S cm⁻¹) (Fig. S13). Compared with the result obtained for the COF pellets, this slight difference in the ionic conductivity could be attributed to the thin COF layer

(~ 600 nm) deposited on the PE separator (~ 20 μm).

The effect of COF@PE on the Li^+ transference number was determined by using the Bruce–Vincent method. The results revealed a higher Li^+ transference number of TB–COF–TFSILi (0.87) compared with those of pristine PE (0.38), TB–COF (0.56) and TB–COF– SO_3Li (0.76) (Fig. 4c, Fig. S14 and Table S2), which can be attributed to the high ionic dissociation and smaller pore size [16,61]. This higher Li^+ transference number can beneficially contribute to increasing the Li^+ conductivity ($=$ ionic conductivity $\times t_{\text{Li}^+}$). The Li^+ conductivities of the TB–COF–TFSILi@PE, TB–COF– SO_3Li @PE, TB–COF@PE and pristine PE were estimated to be 3.28×10^{-4} , 2.81×10^{-4} , 2.00×10^{-4} and 2.70×10^{-4} S cm^{-1} , respectively. Consequently, the difference between these membranes was more pronounced for the Li^+ conductivity compared with the ionic conductivity shown in Fig. S13.

To investigate the effect of the COF@PEs on the redox reactions of Li–S cells, cyclic voltammetry (CV) experiments were conducted in the potential range of 1.65–2.65 V vs. Li/Li^+ at a scan rate of 0.1 mV s^{-1} (Fig. 4d). The positions of two oxidation and two reduction peaks, corresponding to the electrochemical conversion reactions [55] between sulfur and $\text{Li}_2\text{S}_2/\text{Li}_2\text{S}$, were analysed. For the TB–COF– SO_3Li , the oxidation peaks appeared at 2.35 and 2.42 V, which were lower than those observed for the TB–COF@PE and TB–COF– SO_3Li @PE, indicating the improved conversion reaction kinetics of polysulfides, potentially due to the catalytic effect [62] of the TB–COF– SO_3Li . Additionally, the height gaps of the main peaks slightly increased with the larger anion size, indicating the improved Li–S battery reversibility of the TB–COF–TFSILi@PE compared with the TB–COF@PE and TB–COF– SO_3Li @PE. Next, the rate capability of the samples was compared to investigate their Li^+ transport effects (Fig. 4e and Fig. S15). The Li–S cell with the TB–COF–TFSILi@PE showed high discharge capacities of 1247, 1169, 1038, 934, 776 and 627 mAh g^{-1} at C-rates of 0.1, 0.2, 0.5, 1, 2 and 5 C, respectively, and the capacity was restored to 1157 mAh g^{-1} when the C-rate was returned to 0.2 C, which were comparable to those of previous works [49,56–58]. In contrast, the Li–S cells with the TB–COF@PE and TB–COF– SO_3Li @PE exhibited notable capacity decay at high rates. These results indicated that the TB–COF–TFSILi@PE contributed to facilitating the charge/discharge reaction kinetics in Li–S cells.

The dependence of the scan rate on the current response was utilized to calculate the Li^+ diffusion

coefficients (D_{Li^+}) by using the Randles–Sevcik equation [63]:

$$I_p = 2.69 \times 10^5 n^{1.5} A D_{\text{Li}^+}^{0.5} C_{\text{Li}^+} v^{0.5},$$

where I_p is the value of the peak current (A), n is the number of transferred electrons ($n = 2$ for LSB), A is the area of active material (cm^2), D_{Li^+} is the diffusion coefficient of Li^+ , C_{Li^+} is the concentration of Li^+ (mol mL^{-1}) and v is the scan rate (V s^{-1}). The D_{Li^+} value was calculated by using a linear fit (Fig. S16 and Table S3). The calculated D_{Li^+} of the peak I_{R2} of the TB–COF–TFSILi@PE was 9.47×10^{-8} $\text{cm}^2 \text{s}^{-1}$, which was nearly two times higher than the D_{Li^+} values of the TB–COF@PE and TB–COF– SO_3Li @PE. This enhancement in D_{Li^+} suggests that the TB–COF–TFSILi@PE facilitates Li^+ transport while mitigating polysulfide crossover. Although not a direct indicator of performance, D_{Li^+} provides useful insight into the balance between Li^+ conduction (permeability) and polysulfide shuttle suppression (selectivity), reflecting the significance of the COF@PE design on Li–S battery operation.

Polysulfide-repellent ability to block the shuttle effect

The PS permeability of the TB–COF–TFSILi@PE membranes was investigated to determine its effectiveness in preventing PS crossover (Fig. 5a). For this measurement, Li_2S_6 was selected as a representative PS component, considering its contribution to the PSs shuttle effect due to its high solubility in the electrolyte [64]. To this end, 0.05 M Li_2S_6 in DOL/DME was prepared in the left chamber, while blank DOL/DME solvent was placed in the right chamber. Within an hour, the pristine PE separator exhibited a vivid jacinth color, indicating the penetration of PSs through the separator at an accelerated rate. After 3 hours, the right chamber was contaminated with vivid scarlet PSs, indicating the failure of the pristine PE to block the penetration of soluble PSs over time. In contrast, there was no distinct change in the color of the TB–COF–TFSILi@PE after 3 days, indicating the effective prevention of PS crossover. Given that conventional separator modification strategies, such as functional coatings incorporating carbon-based or inorganic or hybrid materials, have typically demonstrated PS suppression for ≤ 24 hours [65,66], this result underscores the excellent polysulfide repulsion capability of the TB–COF–TFSILi@PE, significantly outperforming conventional approaches.

Self-discharge is a major issue of Li–S batteries that is typically caused by the shuttle effect, as it leads to reduced shelf life, inferior electrochemical

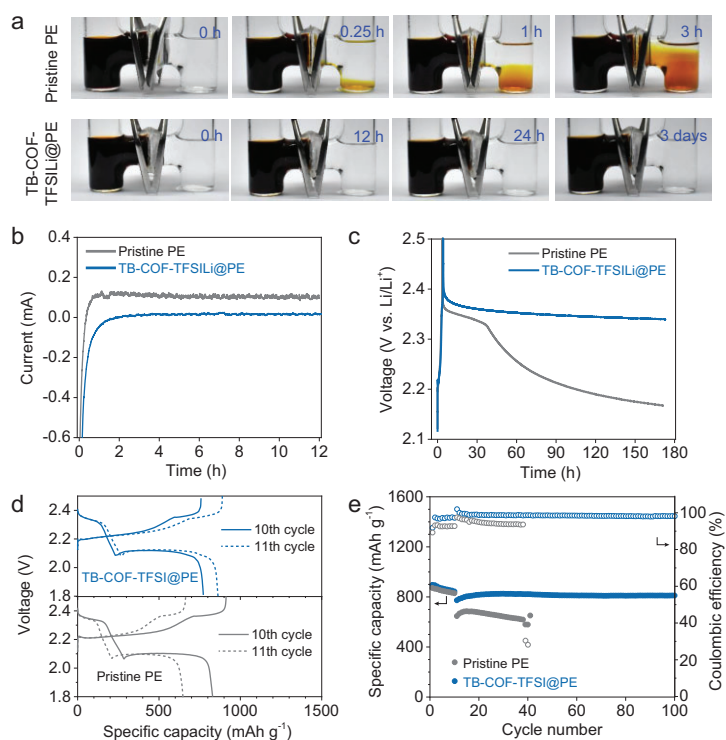


Figure 5. Polysulfide-repellent ability to block the shuttle effect. (a) Digital photographs of polysulfide diffusion of H-type glass cells separated by (top) pristine PE and (bottom) the TB-COF-TFSiLi@PE. (b) Shuttle current measurement with the pristine PE and TB-COF-TFSiLi@PE without the LiNO₃ additive. (c) Self-discharge test of charged Li-S cells over a 7-day rest period. The cells were cycled at 0.2 C for 10 cycles and then charged to 2.5 V. (d) Charge/discharge voltage profiles of the cells before and after the rest period (between the 10th and 11th cycles): (top) TB-COF-TFSiLi@PE and (bottom) pristine PE. The solid line represents the 10th cycle and the dashed line represents the 11th cycle. (e) Comparison of capacity retention after the self-discharge test with the COF@PEs.

performance and coulombic efficiency, and depletion of energy [10]. The shuttle currents of COF@PEs were measured to quantify their effectiveness in blocking PS shuttling (Fig. 5b). In this experiment, the current decay correlates with the PS consumption at the Li-metal anode. The cell with the TB-COF-TFSiLi@PE exhibited a lower current magnitude of 17 μ A after 12 hours compared with that of the pristine PE (100 μ A at 2.38 V vs. Li/Li⁺). These results further confirmed the effectiveness of the TB-COF-TFSiLi@PE in preventing PS shuttling, as denoted by the negligible conversion of higher-order PS into lower-order PS at the Li-metal anode. The self-discharging phenomena were further investigated by measuring the open circuit voltage (OCV) over time (Fig. 5c). The Li-S cells were galvanostatically charged and discharged at a rate of 0.2 C for 10 cycles, after which they were charged to 2.5 V vs. Li/Li⁺ and left to rest for a week. The OCV of the cell with pristine PE decreased to 2.17 V vs. Li/Li⁺ after a week. In contrast, the cell with the TB-COF-TFSiLi@PE exhibited excellent anti-self-discharge performance, as it maintained a

high potential of 2.34 V vs. Li/Li⁺. To verify this advantageous effect, the discharge capacities of the cells were compared after 1 week (between the 10th and 11th cycles) to determine the capacity loss possibly caused by the self-discharge (Fig. 5d). The capacity loss of the cell with the pristine PE (22.9%) was significantly higher than that of the cell with the TB-COF-TFSiLi (8.3%). During the subsequent cycles, the cell with the TB-COF-TFSiLi@PE maintained stable cycle performance (Fig. 5e), whereas the cell with the pristine PE showed rapid capacity decline. The slight increase in the capacity during the subsequent cycles could be attributed to the reactivation of the PSs trapped by the TB-COF-TFSiLi@PE, which was in line with the previously reported results [67]. These results confirm the electrochemical viability of the TFSi⁻-containing COF in mitigating the self-discharge problem of Li-S cells.

Electrochemical performance of the Li-S cells with the TB-COF-TFSiLi@PE

The cycling performance of the Li-S cells with the pristine PE and TB-COF-TFSiLi@PE was evaluated at 0.2 C. After 250 cycles, the cell with the TB-COF-TFSiLi@PE exhibited a higher capacity retention of 92.6%, whereas the cell with pristine PE retained only 57.2% of its original capacity after 100 cycles (Fig. 6a). The TB-COF-TFSiLi@PE exhibited excellent electrochemical performance, with 0.034% decay per cycle. It should be noted that the decay per cycle of the TB-COF-TFSiLi@PE at a discharge rate of 0.2 C is lower than those of previously reported Li-S cells (Table S4). This finding is significant because the capacity degradation rate of Li-S cells typically increases at lower current densities, indicating that the TB-COF-TFSiLi can effectively mitigate the shuttle effect while facilitating Li⁺. Additionally, the TB-COF-TFSiLi@PE achieved superior cycling retention even at a faster current charge/discharge rate of 2.0 C (Fig. S17). To explore the practical feasibility of the TB-COF-TFSiLi, Li-S cells were fabricated by pairing thin (50 μ m) Li-metal anodes and high-S-loading (ranging from 3.6 to 8.3 mg cm⁻²) cathodes in a lean electrolyte (4.5 μ L g_{sulfur}⁻¹). Under these stringent cell conditions, the cells showed an increase in the areal capacity that was proportional to the S loading, while maintaining stable cycling performance over all of the S loadings (Fig. 6b). Additionally, the applicability of the TB-COF-TFSiLi was demonstrated in pouch-type Li-S cells (areal capacity = 4.5 mAh cm⁻², electrode size = 3 \times 3 cm²) fabricated under practical yet challenging conditions, including high sulfur loading (5.2 mg cm⁻²), a thin Li-metal anode (50 μ m) and a lean electrolyte (4.5 μ L g_{lithium}⁻¹)

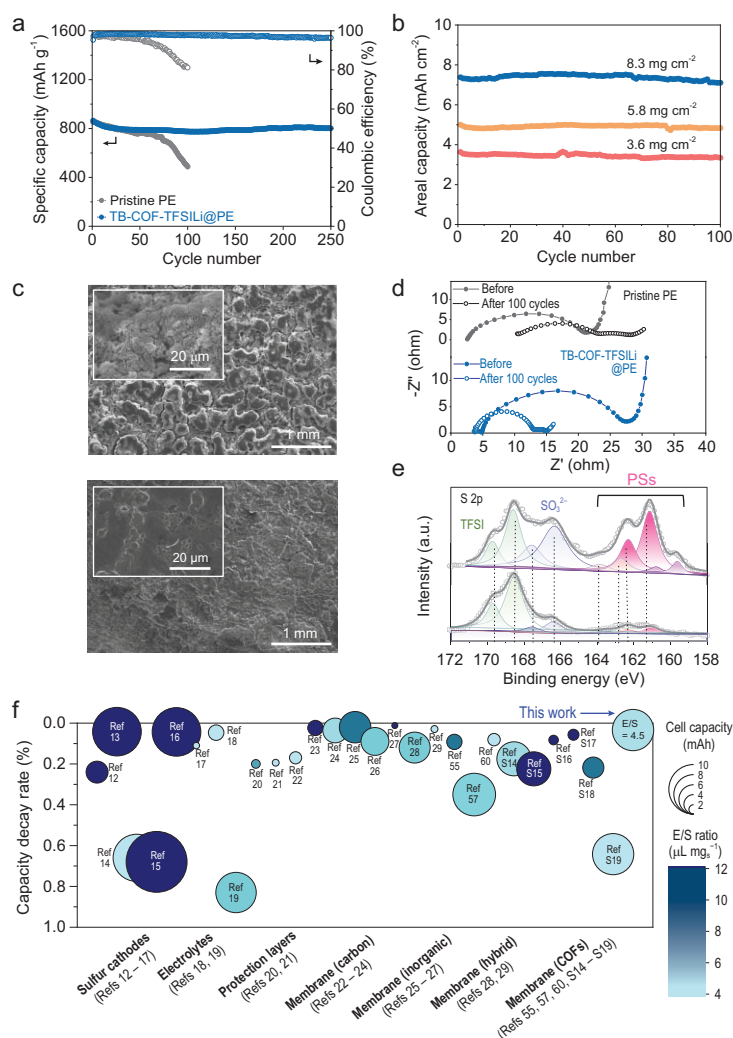


Figure 6. Electrochemical performance of the Li-S cells with the TB-COF-TFSILi@PE. (a) Cycling retention of the Li-S cells with the TB-COF-TFSILi@PE (vs. pristine PE) at charge/discharge current densities of 0.2 C/0.2 C (S loading = 2.25 mg cm⁻²; E/S ratio = 10 $\mu\text{L mg}_{\text{sulfur}}^{-1}$). (b) Cycling retention of the Li-S with the TB-COF-TFSILi@PE at charge/discharge current density of 0.1 C/0.1 C and E/S ratio = 4.5 $\mu\text{L mg}_{\text{sulfur}}^{-1}$ as a function of S loading. (c) Surface SEM images of the Li-metal anodes after 100 cycles, in which the Li-S cells were fully discharged: (top) pristine PE and (bottom) TB-COF-TFSILi@PE. (d) EIS spectra of the Li-S cells with (top) pristine PE and (bottom) TB-COF-TFSILi@PE before and after 100 cycles. (e) S 2p XPS spectra and the associated composition analysis of the Li-metal anodes after 100 cycles: (top) pristine PE and (bottom) TB-COF-TFSILi@PE. (f) Comparison of Li-S cell with the TB-COF-TFSILi@PE (this study) and previously reported Li-S cells, with a focus on the capacity decay rate, cell capacity (area) and E/S ratio (heat map).

(Fig. S18 and Table S6). The resulting pouch cell with the TB-COF-TFSILi@PE exhibited a high cathode capacity of 40.5 mAh along with stable cycling retention. These results underscore the electrochemical reliability of the TB-COF-TFSILi-based membranes, particularly in enhancing the long-term cycling stability of Li-S cells.

The beneficial effect of the TB-COF-TFSILi@PE on the cycling performance was verified

by performing a post-mortem analysis of the cycled Li-S cells. The cycled Li-metal anodes (after 100 cycles) were analysed by using SEM images to evaluate the effectiveness of the TB-COF-TFSILi in Li-stripping/plating reversibility. When the pristine PE was used, the cycled Li-metal anode exhibited a porous morphology, with its surface randomly covered with dead Li (Fig. 6c, top). In contrast, the cycled Li-metal anode showed a comparatively smoother morphology when the TB-COF-TFSILi@PE was used (Fig. 6c, bottom). Given that a high Li⁺ transference number promotes uniform Li⁺ diffusion and stable Li deposition by mitigating space-charge formation, the charge/discharge reversibility of Li might be enhanced in the cell containing the TB-COF-TFSILi@PE [68]. To provide additional evidence, the electrochemical impedance spectroscopy (EIS) spectra of the cycled Li-S cells were analysed (Fig. 6d and Fig. S19). After 100 cycles, the bulk electrolyte resistance (R_b) of the TB-COF-TFSILi@PE was negligibly changed, whereas a significant increase in the R_b value was observed in the pristine PE. The increase in the R_b of Li-S cells might be due to electrolyte depletion resulting from the formation of Li dendrites and dead Li in the Li anode [69]. Moreover, the electrode-electrolyte interfacial resistance (R_{int}) and charge-transfer resistance (R_{ct}) of the TB-COF-TFSILi@PE were lower than those of the pristine PE, indicating the stabilized electrode-electrolyte interface enabled by the TB-COF-TFSILi@PE. Meanwhile, the decrease in the R_{int} and R_{ct} values after the cycling test could be attributed to the relocation of sulfur active materials during the phase transition [70].

Next, XPS was employed to further elucidate the chemical composition of the cycled Li surface (Fig. 6e). The characteristic S 2p_{3/2} peaks observed at <165 eV can be attributed to the decomposition byproduct of PS, whereas the peaks at >165 eV were derived from TFSI⁻ anions from salts containing oxide or sulfoxide [44,45]. The cell with pristine PE exhibited a significantly stronger peak intensity of the insoluble Li₂S₂/Li₂S layer compared with the cell with the TB-COF-TFSILi@PE. To assess the degree of the parasitic reactions of PSs, the atomic content on Li-metal anodes was investigated by using XPS analysis (Fig. S20) and the results revealed that the atomic S content on the Li-metal anodes with the TB-COF-TFSILi@PE (0.8 at% S) was lower than that on the anode with pristine PE (2.1 at% S). Additionally, the atomic Li content was higher on the Li anode with the TB-COF-TFSILi@PE (43.8 at% Li) than that with pristine PE (29.7 at% Li), indicating the effective inhibition of the parasitic reactions of PSs by the TB-COF-TFSILi@PE. Meanwhile, the structural stability of

the TB-COF-TFSiLi@PE was analysed before and after 100 cycles (Fig. S21). No significant changes in the FT-IR spectra were observed in the characteristic peaks of νCH_2 and $\nu\text{C}=\text{N}$, demonstrating that the TB-COF-TFSiLi maintained its structural integrity during the cycling test.

A comparative analysis with previously reported Li-S cells was performed to demonstrate the advantageous effects of the TB-COF-TFSiLi@PE (Table S5), with a focus on selectivity (capacity decay rate) and permeability (cell capacities and E/S ratios). Maintaining high capacities at low E/S ratios is essential for achieving practical energy-dense Li-S cells. The TB-COF-TFSiLi@PE achieved an exceptionally low rate of capacity decay (0.046%) under stringent cell conditions (8.3 mAh and E/S ratio of $4.5\ \mu\text{L mg}_{\text{sulfur}}^{-1}$) (Fig. 6b), whereas most of the previous works—including S cathode modifications [12–17], electrolyte formulations [18,19], protective layers [20,21], various membranes [22–29], even those incorporating COFs [55,56,59]—showed high rates of capacity decay under non-practical cell operating conditions (low capacities and high E/S ratios) (Fig. 6f). Given that the reversible electrochemical conversion reaction of S is hindered under lean electrolyte conditions, this study underscores the pivotal role of the TB-COF-TFSiLi@PE in facilitating the electrostatic permselective effect, thereby enhancing conversion kinetics and preventing the PS shuttle effect. These advancements collectively contribute to improved electrochemical cycling performance and energy densities in Li-S cells.

CONCLUSION

In summary, we have presented the ion channel-gated COF as an ionic diode membrane designed to resolve the conflicting challenge between shuttle prevention and Li^+ conduction in Li-S batteries. The bulky anion (TFSi^-)-tethered COF channels delocalized the negative charge sites and reduced the pore size, thereby repelling the PSs through a combination of electrostatic interaction and steric hindrance. Consequently, the TB-COF-TFSiLi@PE effectively mitigated the shuttle effect without impairing Li^+ transport, in contrast to the TB-COF- SO_3Li @PE. Moreover, the TB-COF-TFSiLi@PE alleviated the self-discharge problem and inhibited the parasitic reactions. Owing to these beneficial effects of the bulky anion-tethered COF, the Li-S cells with the TB-COF-TFSiLi@PE exhibited improved cycling retention (decay rate = 0.034% per cycle vs. pristine PE separator = 0.428%). Particularly, the TB-COF-TFSiLi@PE enabled the realization of practical high-energy-density Li-S cells under constrained conditions. Beyond Li-S batteries, the

ion channel-gated COF, with its charge-delocalized and size-tuned pores, holds promise as a platform technology for next-generation rechargeable batteries. Its selective ion-transport mechanism not only suppresses side reactions, but also ensures efficient ion conduction, making it applicable to Li-ion and metal-sulfur batteries, including those based on sodium, potassium, magnesium and aluminum. These properties highlight its potential as a versatile membrane for advanced energy-storage systems.

SUPPLEMENTARY DATA

Supplementary data are available at [NSR](https://doi.org/10.1093/nsr/nwaf193) online.

FUNDING

This work was supported by the Basic Science Research Program (RS-2024-00344021, RS-2023-00261543 and 2021M3H4A1A02099355) through the National Research Foundation of Korea (NRF) grant by the Korean Government (MSIT), the National Research Council of Science & Technology (NST) grant by the Korea Government (MSIT) (GTL24011-000), and Korea Institute for Advancement of Technology (KIAT) grant funded by the Korea Government (MOTIE) (RS-2024-00420590, HRD Program for Industrial Innovation). This work was also supported by Yonsei University Research Fund of 2020-22-0536. The computational work was supported by the Supercomputing Center/Korea Institute of Science and Technology Information with supercomputing resources, including technical support (KSC-2022-CHA-0007 to D.-H. S.).

AUTHOR CONTRIBUTIONS

Z.L., S.P. and H.M. conducted main experiments and data collection. J.-S. K. conducted the DFT simulation. H. M., K.-S. O., Y. H., K. R., C. Li, J.-M. Seo, X. L. and J.-B. B. conducted supporting experiments and discussion. S.-Y. L. coordinated and supervised the overall project. Z. L., S. P., D.-H. S. and S.-Y. L. wrote the manuscript and all authors discussed the result and commented on the manuscript.

Conflict of interest statement. None declared.

REFERENCES

- Asl HY and Manthiram A. Toward sustainable batteries. *Nat Sustain* 2021; **4**: 379–80.
- Yue L, Wang D, Wu Z *et al.* Polyrrole-encapsulated Cu_2Se nanosheets in situ grown on Cu mesh for high stability sodium-ion battery anode. *Chem Eng J* 2022; **433**: 134477.
- Yue L, Ma C, Yan S *et al.* Improving the intrinsic electronic conductivity of NiMoO_4 anodes by phosphorous doping for high lithium storage. *Nano Res* 2022; **15**: 186–94.
- Manthiram A, Fu Y, Chung S-H *et al.* Rechargeable lithium-sulfur batteries. *Chem Rev* 2014; **114**: 11751–87.

5. Zhao W, Ma X, Gao L *et al.* Hierarchical architecture engineering of branch-leaf-shaped cobalt phosphosulfide quantum dots: enabling multi-dimensional ion-transport channels for high-efficiency sodium storage. *Adv Mater* 2024; **36**: 2305190.
6. Seh Z, Sun Y, Zhang Q *et al.* Designing high-energy lithium-sulfur batteries. *Chem Soc Rev* 2016; **45**: 5605–34.
7. Pang Q, Liang X, Kwok C *et al.* Advances in lithium-sulfur batteries based on multifunctional cathodes and electrolytes. *Nat Energy* 2016; **1**: 16132.
8. Evers S and Nazar L. New approaches for high energy density lithium-sulfur battery cathodes. *Acc Chem Res* 2013; **46**: 1135–43.
9. Xiao R, Yang S, Yu T *et al.* A Janus separator for inhibiting shuttle effect and lithium dendrite in lithium-sulfur batteries. *Batteries & Supercaps* 2022; **5**: e202200101.
10. Li S, Zhang W, Zheng J *et al.* Inhibition of polysulfide shuttles in Li-S batteries: modified separators and solid-state electrolytes. *Adv Energy Mater* 2021; **11**: 2000779.
11. Yang S, Xiao R, Hu T *et al.* Ni₂P electrocatalysts decorated hollow carbon spheres as bi-functional mediator against shuttle effect and Li dendrite for Li-S batteries. *Nano Energy* 2021; **90**: 106584.
12. Cai W, Li G, Zhang K *et al.* Conductive nanocrystalline niobium carbide as high-efficiency polysulfides tamer for lithium-sulfur batteries. *Adv Funct Mater* 2018; **28**: 1704865.
13. Huang Y, Shaibani M, Gamot DT *et al.* A saccharide-based binder for efficient polysulfide regulations in Li-S batteries. *Nat Commun* 2021; **12**: 5375.
14. Wang H, Ling M, Bai Y *et al.* Cationic polymer binder inhibit shuttle effects through electrostatic confinement in lithium sulfur batteries. *J Mater Chem A* 2018; **6**: 6959–66.
15. Zhang L, Ling M, Feng J *et al.* Effective electrostatic confinement of polysulfides in lithium/sulfur batteries by a functional binder. *Nano Energy* 2017; **40**: 559–65.
16. Lee B-J, Kang T-H, Lee H-Y *et al.* Revisiting the role of conductivity and polarity of host materials for long-life lithium-sulfur battery. *Adv Energy Mater* 2020; **10**: 1903934.
17. Liu W, Liu M, Shen H *et al.* Insights into nickel nanoparticles modified porous biomass-derived carbon as sulfur host matrix for advanced rechargeable lithium-sulfur battery. *J Alloys Compd* 2023; **937**: 168459.
18. Yanagi M, Ueno K, Andoet A *et al.* Effects of polysulfide solubility and Li ion transport on performance of Li-S batteries using sparingly solvating electrolytes. *J Electrochem Soc* 2020; **167**: 070531.
19. Zheng J, Fan X, Ji G *et al.* Manipulating electrolyte and solid electrolyte interphase to enable safe and efficient Li-S batteries. *Nano Energy* 2018; **50**: 431–40.
20. Guo W, Han Q, Jiao J *et al.* In situ construction of robust biphasic surface layers on lithium metal for lithium-sulfide batteries with long cycle life. *Angew Chem* 2021; **133**: 7343–50.
21. Yao Y, Zhang X, Li B *et al.* A compact inorganic layer for robust anode protection in lithium-sulfur batteries. *InfoMat* 2020; **2**: 379–88.
22. Singhal R, Chung S, Manthiram A *et al.* A free-standing carbon nanofiber inter-layer for high-performance lithium-sulfur batteries. *J Mater Chem A* 2015; **3**: 4530–8.
23. Lee HD, Ahn HJ, Park M-S *et al.* Metal-organic framework/carbon nanotube-coated polyethylene separator for improving the cycling performance of lithium-sulfur cells. *Electrochim Acta* 2018; **283**: 1291–9.
24. Wang Z, Feng M, Sun H *et al.* Constructing metal-free and cost-effective multifunctional separator for high-performance lithium-sulfur batteries. *Nano Energy* 2016; **20**: 176–84.
25. Lv X, Lei T, Wang B *et al.* An efficient separator with low Li-ion diffusion energy barrier resolving feeble conductivity for practical lithium-sulfur batteries. *Adv Energy Mater* 2019; **9**: 1901800.
26. Zuo Y, Zhu Y, Tang X *et al.* MnO₂ supported on acrylic cloth as functional separator for high-performance lithium-sulfur batteries. *J Power Sources* 2020; **464**: 228181.
27. Sun Z, Wang T, Zhang Y *et al.* Boosting the electrochemical performance of lithium/sulfur batteries with the carbon nanotube/Fe₃O₄ coated by carbon modified separator. *Electrochim Acta* 2019; **327**: 134843.
28. Yu Z, Wang B, Liao X *et al.* Boosting polysulfide redox kinetics by graphene-supported Ni nanoparticles with carbon coating. *Adv Energy Mater* 2020; **10**: 2000907.
29. Wu J, Zeng H, Li X *et al.* Ultralight layer-by-layer self-assembled MoS₂-polymer modified separator for simultaneously trapping polysulfides and suppressing lithium dendrites. *Adv Energy Mater* 2018; **8**: 1802430.
30. Waller JP, Gándara F, Yaghi MO. Chemistry of covalent organic frameworks. *Acc Chem Res* 2015; **48**: 3053–63.
31. Geng K, He T, Liu R *et al.* Covalent organic frameworks: design, synthesis, and functions. *Chem Rev* 2020; **120**: 8814–933.
32. Kandambeth S, Dey K, Banerjee R *et al.* Covalent organic frameworks: chemistry beyond the structure. *J Am Chem Soc* 2019; **141**: 1807–22.
33. Lohse SM and Bein T. Covalent organic frameworks: structures, synthesis, and applications. *Adv Funct Mater* 2018; **28**: 1705553.
34. Zhao X, Pachfule P, Thomas A *et al.* Covalent organic frameworks (COFs) for electrochemical applications. *Chem Soc Rev* 2021; **50**: 6871–913.
35. Li J, Jing X, Li Q *et al.* Bulk COFs and COF nanosheets for electrochemical energy storage and conversion. *Chem Soc Rev* 2020; **49**: 3565–604.
36. Liang X, Tian Y, Yuan Y *et al.* Ionic covalent organic frameworks for energy devices. *Adv Mater* 2021; **33**: 2105647.
37. Liu Z, Zhang K, Huang G *et al.* Highly processable covalent organic framework gel electrolyte enabled by side-chain engineering for lithium-ion batteries. *Angew Chem Int Ed* 2022; **6**: e202110695.
38. Hu Y, Dunlap N, Wan S *et al.* Crystalline lithium imidazolate covalent organic frameworks with high Li-ion conductivity. *J Am Chem Soc* 2019; **141**: 7518–25.
39. Duan H, Li K, Xie M *et al.* Scalable synthesis of ultrathin polyimide covalent organic framework nanosheets for high-performance lithium-sulfur batteries. *J Am Chem Soc* 2021; **143**: 19446–53.
40. Xu J, Tang W, Yang C *et al.* A highly conductive COF@CNT electrocatalyst boosting polysulfide conversion for Li-S chemistry. *ACS Energy Lett* 2021; **6**: 3053–62.
41. Li P, Lv H, Li Z *et al.* Li, X. The electrostatic attraction and catalytic effect enabled by ionic-covalent organic nanosheets on MXene for separator modification of lithium-sulfur batteries. *Adv Mater* 2021; **33**: 2007803.
42. Halder S, Wang M, Bhauriyal P *et al.* Porous dithiine-linked covalent organic framework as a dynamic platform for covalent polysulfide anchoring in lithium-sulfur battery cathodes. *J Am Chem Soc* 2022; **144**: 9101–12.
43. Liao H, Ding H, Li B *et al.* Covalent-organic frameworks: potential host materials for sulfur impregnation in lithium-sulfur batteries. *J Mater Chem A* 2014; **2**: 8854–8.
44. Ghazi AZ, Zhu L, Wang H *et al.* Efficient polysulfide chemisorption in covalent organic frameworks for high-performance lithium-sulfur batteries. *Adv Energy Mater* 2016; **6**: 1601250.
45. Li X, Zhang K, Yuan Y *et al.* Constructing ambivalent imidazopyridinium-linked covalent organic frameworks. *Nat Synth* 2022; **1**: 382–92.

46. Wang Q, Tang K, Liao Q *et al*. In situ deformation topology of COFs with shortened channels and high redox properties for Li-S batteries. *Adv Funct Mater* 2023; **33**: 2211356.
47. Guo C, Liu M, Gao G *et al*. Anthraquinone covalent organic framework hollow tubes as binder microadditives in Li-S batteries. *Angew Chem Int Ed* 2022; **61**: e202113315.
48. Liu W, Gong L, Liu Z *et al*. Conjugated three-dimensional high-connected covalent organic frameworks for lithium-sulfur batteries. *J Am Chem Soc* 2022; **144**: 17209–18.
49. Xu J, An S, Song X *et al*. Towards high performance Li-S batteries via sulfonate-rich COF-modified separator. *Adv Mater* 2021; **33**: 2105178.
50. Cao Y, Wu H, Li G *et al*. Ion selective covalent organic framework enabling enhanced electrochemical performance of lithium-sulfur batteries. *Nano Lett* 2021; **21**: 2997–3006.
51. Hu B, Xu J, Fan Z *et al*. Covalent organic framework based lithium-sulfur batteries: materials, interfaces, and solid-state electrolytes. *Adv Energy Mater* 2023; **13**: 2203540.
52. Chen D, Huang S, Zhong L *et al*. In situ preparation of thin and rigid COF film on Li anode as artificial solid electrolyte interphase layer resisting Li dendrite puncture. *Adv Funct Mater* 2020; **30**: 1907717.
53. Chen H, Tu H, Hu C *et al*. Cationic covalent organic framework nanosheets for fast Li-ion conduction. *J Am Chem Soc* 2018; **140**: 896–9.
54. Vazquez-Molina AD, Mohammad-Pour SG, Lee C *et al*. Mechanically shaped two-dimensional covalent organic frameworks reveal crystallographic alignment and fast Li-ion conductivity. *J Am Chem Soc* 2016; **138**: 9767–70.
55. Wang M, Emre EA, Ji K *et al*. Multifactorial engineering of biomimetic membranes for batteries with multiple high-performance parameters. *Nat Commun* 2022; **13**: 278.
56. Zhang K, Li X, Ma L *et al*. Fluorinated covalent organic framework-based nanofluidic interface for robust lithium-sulfur batteries. *ACS Nano* 2023; **17**: 2901–11.
57. Gao G, Wang Y, Zhu H *et al*. Rapid production of metal–organic frameworks based separators in industrial-level efficiency. *Adv Sci* 2020; **7**: 2002190.
58. An Q, Wang L, Zhao G *et al*. Constructing cooperative interface via bi-functional COF for facilitating the sulfur conversion and Li⁺ dynamics. *Adv Mater* 2024; **36**: 2305818.
59. Han D, Sun L, Li Z *et al*. Supramolecular channels via crown ether functionalized covalent organic frameworks for boosting polysulfides conversion in Li-S batteries. *Energy Storage Mater* 2024; **65**: 103143.
60. Carrigy BN, Pant ML, Mitra S *et al*. Knudsen diffusivity and permeability of PEMFC microporous coated gas diffusion layers for different polytetrafluoroethylene loadings. *J Electrochem Soc* 2013; **160**: F81.
61. Bai S, Sun Y, Yi J *et al*. High-power Li-metal anode enabled by metal-organic framework modified electrolyte. *Joule* 2018; **2**: 2117–32.
62. Guo T, Ding Y, Xu C *et al*. High crystallinity 2D π -d conjugated conductive metal-organic framework for boosting polysulfide conversion in lithium-sulfur batteries. *Adv Sci* 2023; **10**: 2302518.
63. Zhou Q, Dong S, Lv Z *et al*. A temperature-responsive electrolyte endowing superior safety characteristic of lithium metal batteries. *Adv Energy Mater* 2020; **10**: 1903441.
64. Liu R, Wei Z, Peng L *et al*. Establishing reaction networks in the 16-electron sulfur reduction reaction. *Nature* 2024; **626**: 98–104.
65. Qu H, Zhang J, Du A *et al*. Multifunctional sandwich-structured electrolyte for high-performance lithium–sulfur batteries. *Adv Sci* 2018; **5**: 1700503.
66. Jia Y, Chen S, Meng X *et al*. Growing electrocatalytic conjugated microporous polymers on self-standing carbon nanotube films promotes the rate capability of Li–S batteries. *Small* 2023; **19**: 2303919.
67. Yang Y and Zhang J. Highly stable lithium-sulfur batteries based on laponite nanosheet-coated celgard separators. *Adv Energy Mater* 2018; **8**: 1801778.
68. Chen L, Li W, Fan L *et al*. Intercalated electrolyte with high transference number for dendrite-free solid-state lithium batteries. *Adv Funct Mater* 2019; **29**: 1901047.
69. Wang J, Yi S, Liu J *et al*. Suppressing the shuttle effect and dendrite growth in lithium-sulfur batteries. *ACS Nano* 2020; **14**: 9819–31.
70. Yan L, Gao X, Thomas PJ *et al*. Ionically cross-linked PEDOT:PSS as a multifunctional conductive binder for high-performance lithium-sulfur batteries. *Sustain Energy Fuels* 2018; **2**: 1574–81.